JOURNAL OF MATERIALS SCIENCE 32 (1997) 3393–3399

Formation and thermal stability of aluminium nanoparticles synthesized via yttrium ion implantation into sapphire

E. M. HUNT, J. M. HAMPIKIAN*
School of Materials Science and Engineering, Georgia Institute of Technology, 778 Atlantic Dr., Atlanta, GA 30332-0245, USA

Yttrium ion implantation of $11\bar{2}3$ alumina resulted in the formation of metallic aluminium–yttrium, face centred cubic ($a_0 = 0.41$ nm) spherical nanocrystals ($\sim$12 nm in diameter) embedded in an amorphous matrix. A fluence of 5×10^{16} Y^+/cm^2 implanted at ambient temperature and accelerating energies of 150 or 170 keV yielded this result. Crystalline nanoparticles were not present in the amorphous matrix for implantations done with identical conditions but lower energy (100 keV). Substrates implanted at 150 keV were annealed in laboratory air for times ranging from 20 to 90 min and temperatures ranging from 1000 to 1400 °C. A clear progression of morphologies resulted from these annealing treatments. A 1000 °C, 90 min anneal produced $\sim$13% recrystallization of the amorphous region and induced the formation of crystallites of a metastable Y–Al alloy. An 1100 °C, 90 min anneal demonstrated $\sim$40% recrystallization of the amorphous region, accompanied by the formation of partially aligned internal grains of Y_2O_3. Electron diffraction shows that the Y–Al alloy crystallites which formed in the 1000 °C anneal are also present at 1100 °C. A highest temperature anneal of 1400 °C, 60 min induced essentially complete recrystallization of the amorphous phase, the dissolution of the metastable Y–Al alloy, the retention of the internal yttria grains, and the formation of partially oriented external grains of yttria resulting from the segregation of yttrium to the substrate surface.

1. Introduction

It is well established that ion implantation can alter the electrical, mechanical and optical properties of a material. For example, the refractive index of a crystalline insulator may be modified as a result of ion implantation-induced amorphization. More complex alterations in the optical response of insulators involve affecting the susceptibility and dielectric constant of the material through the formation of colloidal particles. It has been demonstrated that particles on the order of 10 nm and smaller dispersed in a dielectric solid exhibit novel optical properties [1–4]. The small size induces electronic conditions which cause the electrons to behave in a non-linear fashion in response to applied electromagnetic fields. These non-linear properties show promise for application in integrated optical device technology and other areas concerned with unconventional optical responses.

The formation of colloidal particles may be achieved using ion implantation and, in many cases, the size and distribution of the particles can be controlled by careful post-implantation annealing treatments [1, 2, 5–8]. The purpose of the present work is to establish and characterize the colloidal microstructure which results from yttrium ion implantation into single crystal alumina, and also to examine the effects of post-implantation annealing on this microstructure. Of particular interest is the formation of aluminium-rich nano-sized particles in the as-implanted state, which has not been previously reported. In similar research (ion implantation into alumina), the implantation-induced formation of particles, comprised predominantly of the implanted species, has been observed [1, 2, 5–8], but the formation of metallic aluminium-rich particles in Al_2O_3 has not been reported even when aluminium is the implanted ion species.

Implantation results in a chemically modified layer which is limited in extent by the range/depth of the implanted ion. In these experiments, the yttrium ions come to rest within approximately the first 100 nm of the substrate (for the 150 keV implant), with the peak of the Gaussian profile at approximately 50 nm [9]. The dimension of the affected layer thus necessitates careful preservation of the implanted surface during sample preparation and testing, and also the use of specialized characterization techniques [10],

* Author to whom correspondence should be addressed.

0022–2461

including analytical electron microscopy, energy filtered transmission electron microscopy and Rutherford backscattering spectrometry.

2. Experimental details

The $1\,1\,\bar{2}\,3$ single crystal alumina substrates (99.99% purity) used in this study were obtained with an optical grade surface polish from Saphikon Inc. The 0.7 mm thick substrates were cut into 10 mm × 10 mm samples and annealed at 1500 °C for 80 h to remove residual polishing damage and ensure a crystalline structure throughout the substrate. The crystallinity of the substrate surface was demonstrated by electron channelling in a scanning electron microscope using a backscattered electron detector and 10 keV electrons. Implantation with singly charged yttrium ions (Y^+) was performed using an ion implanter coupled with a high vacuum end station, with the pressure during implantation maintained below $\approx 5 \times 10^{-6}$ Pa. The accelerating potential was selected to be either 100, 150 or 170 kV and yielded Y^+ ions at the corresponding energies. Each substrate received a fluence of 5×10^{16} yttrium ions per square centimetre measured with a Farady cup, and was implanted on one side only. In order to minimize beam heating, substrates were attached to water-cooled copper heat sinks. Post-implantation annealing treatments were carried out in flowing laboratory air at 1000, 1100, 1250 and 1400 °C for times ranging from 20 to 90 min. The samples were placed, implanted surface up, onto a high purity polycrystalline alumina support plate and put in the furnace after it had stabilized at the appropriate temperature.

Rutherford backscattering spectroscopy (RBS) and ion channelling (RBS-C) with a 1.5 MeV beam of $^4He^+$ was used to examine the laterally averaged chemical profile of yttrium versus energy (depth below the implanted surface) and the implantation-induced damage to the crystalline lattice. These experiments were carried out at the Oak Ridge National Laboratory Surface Modification and Characterization Facility (SMaC Facility). The extent of this damage was further investigated through Knoop microhardness measurements which were carried out in accordance with the ASTM standard for microhardness testing (E 384-89), employing a Lecco DM-400 hardness tester. Scanning electron microscopy was also used to examine the implanted surfaces. The implanted surface microstructures and chemical compositions of selected samples were examined with 200 keV electrons in a field emission gun transmission electron microscope (TEM) equipped with an energy dispersive X-ray spectrometer (EDX). The metallic nature of the as-implanted microstructural features was established with energy filtered transmission electron microscopy (EFTEM) by using a 5 eV energy window to isolate the aluminium metal plasmon loss peak at ~15 eV. This analysis was carried out at Oak Ridge National Laboratory through the Shared Equipment Research (SHaRE) programme.

3. Results and discussion

3.1. As-implanted condition

Yttrium ions implanted into $(1\,1\,\bar{2}\,3)$ alumina at energies of 100, 150 and 170 keV to a fluence of 5×10^{16} Y^+/cm^2 produced alumina surfaces which were light bronze in colour. Typical RBS spectra are presented in Fig. 1, obtained from alumina implanted with yttrium at 150 keV. The spectrum labelled "aligned" was collected from a sample which was oriented to allow channelling, seen by the lower yield at low energies. At the aluminium edge, however, the aligned spectrum is dechannelled, indicating the presence of heavily damaged material in the surface region. The thickness of the damaged layer is ~120 nm, calculated using a depth calibration based on the stopping power of alumina. To determine the extent of this damage, Knoop microhardness values were recorded for the three implanted surfaces as well as the unimplanted back-surfaces of the same samples. These values are presented in Fig. 2 as a plot of load versus normalized hardness (unimplanted hardness/implanted hardness). The as-implanted surface hardnesses for all three samples are lower than that of unimplanted substrate material, as indicated by the near surface (low load) normalized hardness values being much less than unity. This corresponds to "absolute softening", which

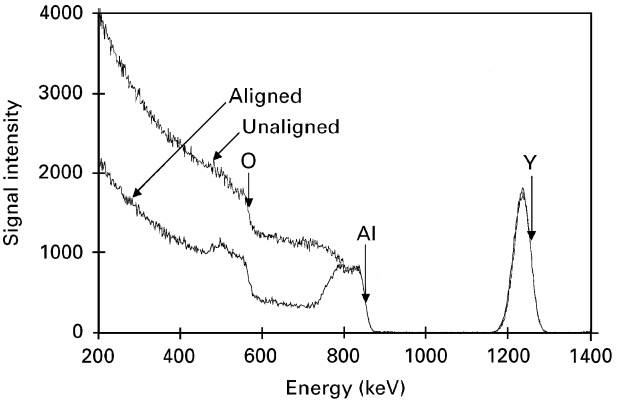

Figure 1 The aligned and unaligned RBS spectra for sapphire implanted with 5×10^{16} Y^+/cm^2 at ambient temperature and an energy of 150 keV.

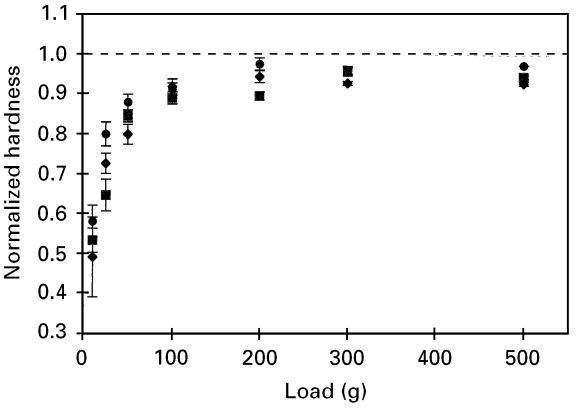

Figure 2 Normalized Knoop hardness values as a function of load for the substrates implanted with Y^+ ions with energies of 100 (●), 150 (■) and 170 keV (◆).

is described in detail by Burnett and Page [11–13], and which, when taken in conjunction with the dechannelled region seen in Fig. 1, indicates the presence of an amorphous region which extends to the sample's surface. This result is in contrast with most of the research done using relatively heavy ions implanted into alumina [6, 14, 15], in which either no amorphous layer is reported for similar and slightly larger ion doses administered at ambient temperature, or the implantations cause the formation of buried amorphous layers.

Transmission electron microscopy of as-implanted plan view samples prepared by polishing and ion milling through the sample's back side to the implanted surface confirmed the presence of amorphous material at the sample surface (see Fig. 3). In addition to the amorphous phase, the existence of lightly diffracting nano-sized crystals ($\approx$12–13 nm) in plan view samples of the two higher energy implants (150 and 170 keV) was also revealed. The nanocrystals are finely distributed and exhibit a face-centred cubic

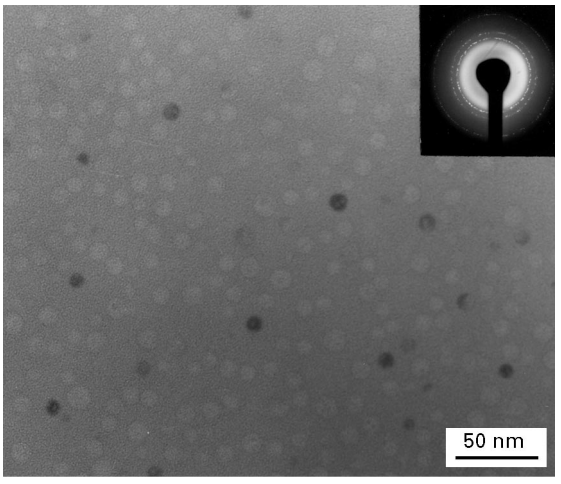

Figure 3 TEM bright field image of particles in the 150 keV as-implanted sample.

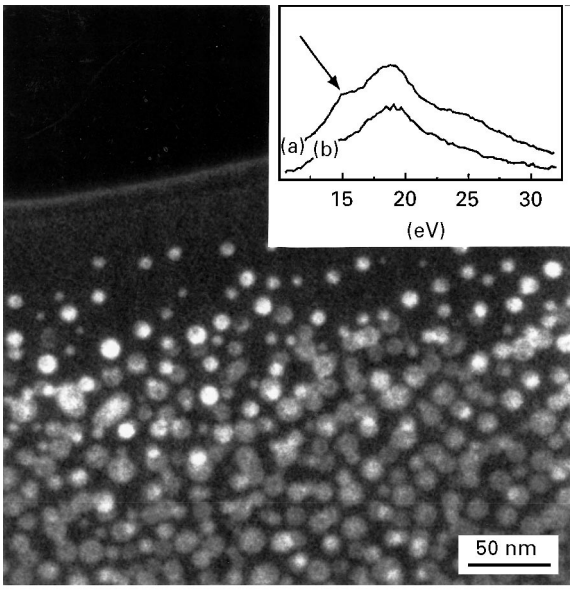

Figure 4 EFTEM image formed using a 5 eV energy window centred on the 15 eV plasmon loss peak associated with metallic aluminium.

structure with a lattice parameter of $a_0 = 0.412 \pm 0.002$ nm [16]. Chemical analysis (EDS) shows qualitatively that these nanocrystals are rich in aluminium and yttrium and poor in oxygen relative to the surrounding amorphous matrix. These are composed of predominantly metallic aluminium, as shown via energy filtered TEM (EFTEM) [17]. A typical image formed using this technique is presented in Fig. 4. Two energy-loss distributions are shown in the inset to Fig. 4; in (a) the spectrum is from an area containing nanocrystals and in (b) the spectrum is from alumina only. The image in Fig. 4 was formed using a 5 eV window centred on the plasmon peak of metallic aluminium (arrowed in the inset of Fig. 4) and appropriate background subtraction [18]. The illuminated particles thus contain metallic aluminium. Further analysis by EFTEM, presented elsewhere [17], confirms that the particles are oxygen deficient in comparison with the matrix material, and that the particles are not yttria. Any measurement of the particle size from Fig. 4 would be imprecise due to the loss of resolution caused by the use of the relatively large 5 eV energy window.

The similarity between the crystallography of the nanocrystals (f c c, $a_0 = 0.412 \pm 0.002$ nm) and that of pure aluminium (f c c, $a_0 = 0.404\,97$ nm), coupled with the qualitative EDS and EFTEM results, indicate that the nanocrystals are predominantly metallic aluminium with a slightly dilated lattice parameter, due to the presence of yttrium. The equilibrium phase diagram predicts negligible solubility of yttrium in aluminium at room temperature [19]. However, ion implantation is a non-equilibrium process and non-equilibrium phases are commonly reported [20]. The mechanism by which the particles form is under further investigation. It appears that the yttrium remains in solid solution, perhaps due to the limited diffusion of yttrium in aluminium at room temperature. Thus, the amount of yttrium in solid solution with aluminium may be estimated using a Vegard's law approach [21]. Such an analysis yields a yttrium concentration of $\sim$7 at %.

The formation of metallic particles due to ion implantation into alumina has been reported by other research groups for implantation which takes place at elevated temperatures. Sklad *et al.* [6] report the formation of 1–3 nm alpha-iron particles after implantation with 1×10^{17} Fe^+/cm^2 at an energy of 160 keV and temperatures ranging from 700–1500 °C. Ohkubo and Suzuki [22] report the formation of Au particles ($<$60 nm) after implantation of 6.8×10^{16} Au^+/cm^2 at an energy of 400 keV and temperature of 1200 °C. The high implantation temperature allows dynamic annealing and diffusion to take place during implantation. Note that in these cases the particles formed were reported to be composed of the implanted ion exclusively. These results contrast with the present research in which the particles are an alloy containing aluminium and yttrium, which were formed by ambient temperature implantation of yttrium. The formation of plate-like metallic aluminium particles has been reported as a result of ion implantation into magnesium spinel at high energy however;

e.g. Ga^+ (ambient temperature, 2.3 MeV) and Al^+ (650 °C, 2.3 MeV) [23].

TEM performed on the 100 keV implanted samples did not reveal the crystalline particles which were present in the higher energy implants, although the amorphous phase was evident from electron diffraction. In order to verify this finding, absorbance spectra of all three implanted samples and an unimplanted alumina standard were recorded, Fig. 5. The absorption feature noted at approximately 24 nm in the spectra from the two particle-bearing samples does not appear in the unimplanted and 100 keV implanted spectra. Since TEM showed the 100 keV sample to contain no crystalline nanoparticles, although it did contain the amorphous phase and an equal amount of yttrium, the absorption appears to be a result of the presence of crystalline Al–Y particles.

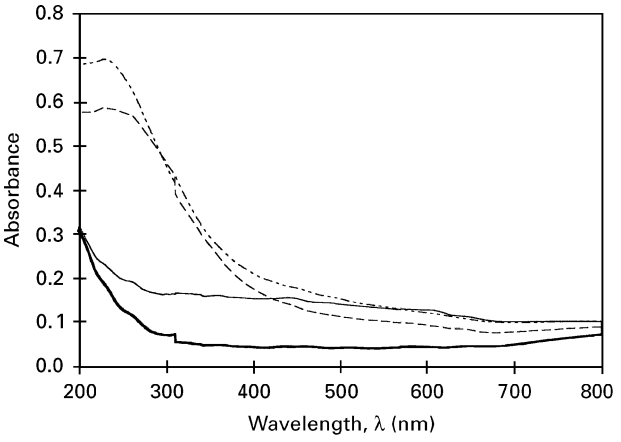

Figure 5 Absorption as a function of incident wavelength for the substrates implanted with Y^+ ions with energies of 100, 150 and 170 keV and a sapphire standard. The discontinuity apparent in the absorption curves at approximately 300 nm is due to an intermittent problem with the spectrophotometer involving an illumination source change. Key: —- - —- - 150 keV implant; – – – 170 keV implant; —— 100 keV implant; —— standard.

3.2. Evolution of microstructure due to annealing

All annealing treatments result in the loss of the bronze coloration due to implantation (substrates revert to transparency). A gradual recrystallization of the damage caused by the implantation was shown by RBS and ion chanelling, as seen in Fig. 6 which contains the aligned aluminium-edge portions of the RBS spectra for the annealed samples. For comparative purposes, the two spectra from Fig. 1 are also present in Fig. 6. The chanelling results are roughly divided into three major groups by similarity in the degree of recrystallization. The approximate average thickness of the dechannelled regions (amorphous regions) for groups 1, 2 and 3 are 100, 45 and 5 nm (essentially totally recrystallized), respectively. Accompanying this gradual recrystallization, there is an evolution in the microstructure of these samples which will be described below. One sample from each recrystallization grouping was chosen to be examined with TEM.

The microstructure of the first sample (implanted at 150 keV, and annealed 90 min at 1000 °C), shown in Fig. 7, contains nano-sized crystals in an amorphous matrix. There are, however, a number of differences relative to the as-implanted case. The annealed crystals are larger than the crystals in the as-implanted case, with an average size of 22 ± 4 nm versus an average as-implanted particle size of 12.5 ± 0.8 nm. The diffraction pattern resulting from an area containing these particles shows a polycrystalline ring pattern, see inset of Fig. 7, that differs from the f c c ring

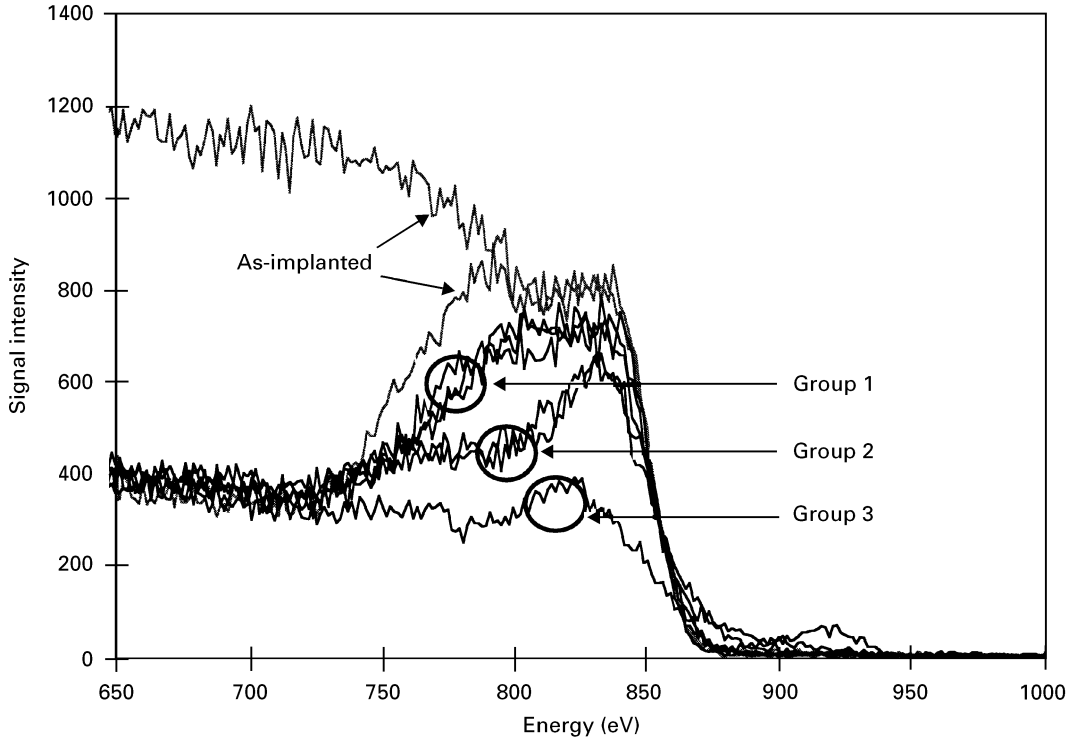

Figure 6 RBS spectra: 150 keV, aligned and unaligned as-implanted and aligned annealed samples.

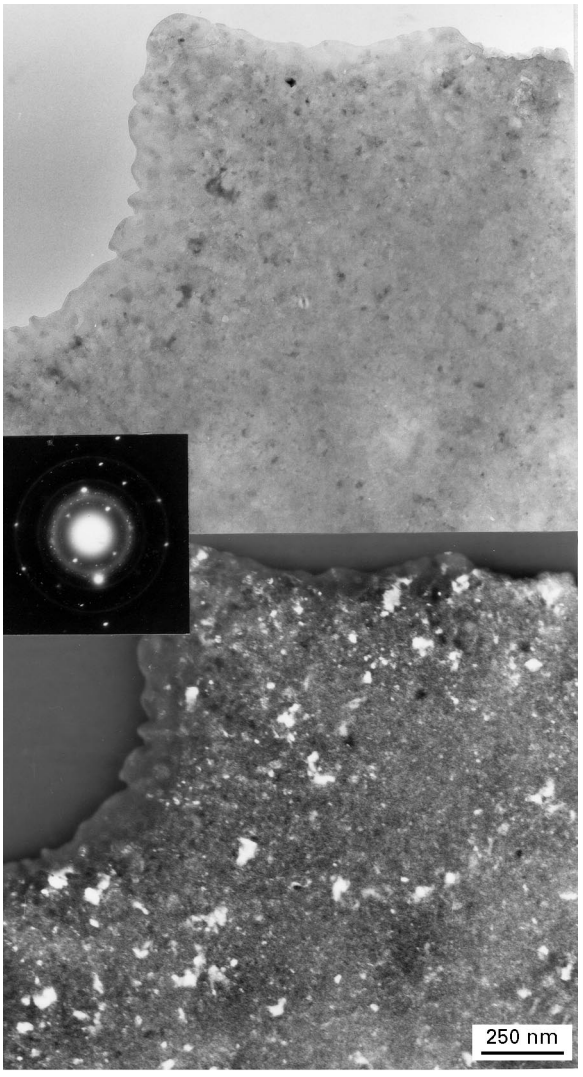

Figure 7 TEM bright and dark field images of the 1000 °C, 90 min annealed sample, and associated diffraction pattern. Dark field image was formed using the indicated portion of the diffraction rings.

pattern found in the as-implanted state (Fig. 3). Using the matrix spots also present in the pattern as an internal standard with which to calibrate the camera length, the *d*-spacings for this new phase were calculated, see Table I. The resulting list of *d*-spacings identify the new material as Y_3Al, a metastable phase with a primitive cubic crystal structure and a lattice parameter of 0.4818 nm, which matches the experimental lattice parameter of 0.481 ± 0.003 nm very well. It should be noted that the fcc implanted particles and the ordered simple cubic metastable particles have an approximately constant amount of aluminium. Assuming $\sim$7% yttrium is present in the as-implanted particles as found by Vegard's analysis the growth of the particles can be accounted for by the increase in yttrium content, presumably by coarsening. There is also the possibility that these crystals could be $Al_5Y_3O_{12}$. This type of phase (usually MAl_2O_4 or $MAlO_3$) is known to form as a result of implantation of Ga, Mn, Ni, Cu, Zn [16], Co [24] and Fe [6] into alumina, followed by annealing. However, the experimental diffraction data support the identification of the metastable Y_3Al phase.

TABLE I Comparison of experimental pattern, Y_3Al and $Al_5Y_3O_{12}$ *d*-spacings (in nm)

Experimental *d*-spacings	Y_3Al *d*-spacings	$Al_5Y_3O_{12}$ *d*-spacings
		0.4905
	0.482	
		0.4247
	0.341	
		0.321
		0.3002
0.278	0.2781	
		0.2687
		0.2561
0.241	0.02409	0.2452
		0.2355
		0.2192
0.207	0.2155	0.2122
0.1917	0.1967	0.1947
		0.1899
		0.1853
		0.177
		0.1733
0.168	0.1703	0.1698
		0.1665
0.162	0.1606	0.1633
		0.1604
0.152	0.1524	0.1524
		0.15
		0.1478
0.148	0.1453	0.1456
		0.1435
		0.1414
0.139	0.1391	0.1396

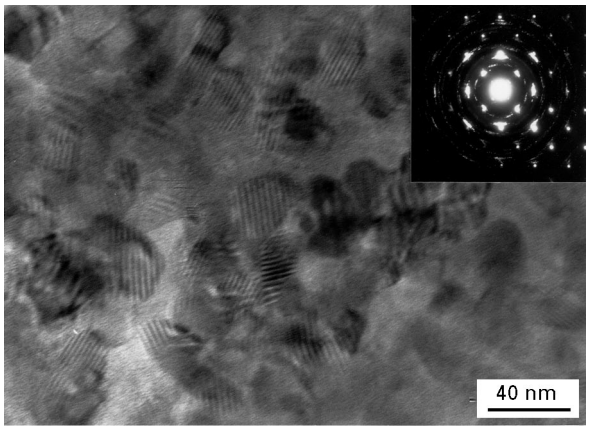

Figure 8 TEM bright field image of the 1100 °C, 90 min annealed sample, and associated diffraction pattern.

The sample from group two which was examined (implanted at 150 keV and annealed 90 min at 1100 °C), represents a large step in the recrystallization process in that the amorphous layer in this sample has been reduced to approximately 40% of its original thickness. There are three separate microstructural elements which comprise this sample, see Fig. 8. Each aspect can be identified through analysis of the associated diffraction pattern, see the inset of Fig. 8. The strong regularly occurring spots represent the recrystallized matrix material. This pattern matches that of the unimplanted substrate material. There are faint, nearly complete rings of spots discernible in this pattern as well. They match the rings of the Y_3Al pattern

seen in Fig. 7. Although the particles are not as evident in the bright field images of this sample, their presence is confirmed by dark field imaging (not shown). Measurements taken from dark field images indicate that these particles range from 8 to 13 nm in diameter. This represents a decrease in particle diameter of approximately 50% relative to the group 1 sample. The arcs adjacent to the matrix spots in the diffraction pattern of Fig. 8 are a result of the formation of irregularly shaped, but oriented Y_2O_3 precipitates, indexed in diffraction as $\{1\,0\,0\}$. The experimental pattern of arcs is the superposition of two $\{1\,0\,0\}$ Y_2O_3 patterns rotated by 90° with respect to each other. The pattern "spots" appear as arcs (not as discrete spots) due to imperfect coherence between the precipitate grains themselves and between the grains and the matrix material. This slight misalignment also causes the Moiré fringes evident in the microstructure.

The group 3 sample which was examined (implanted at 150 keV and annealed 60 min at 1400 °C) has a microstructure and diffraction pattern very similar to those discussed for the previous sample, with two significant differences, see Fig. 9. First, the polycrystalline rings indicating the presence of the randomly oriented Y_3Al precipitates are now absent from the diffraction pattern, inset Fig. 9a. Second, TEM examination reveals the presence of two new forms of precipitate; one large and relatively square, the other elongated. The elongated grains have aspect ratios ranging from 1:1.5 to 1:5. Both precipitate types are faceted and appear to be highly oriented with respect to the surrounding grains. Dark field imaging of this sample shows that the surface precipitates grow with their facets parallel to one of the two unique [4 0 0] directions. High resolution imaging was possible on the elongated surface precipitates and shows that they are highly oriented with respect to the matrix, see Fig. 10. EDS on similar precipitates indicates that they are chemically virtually identical to the Y_2O_3 grains seen in the substrate interior (those which show Moiré contrast). The diffraction pattern for this sample shows no additional features which could be caused by a new phase. The chemical and diffraction evidence, therefore, indicate that these surface precipitates are also Y_2O_3. These precipitates can also be seen with scanning electron microscopy (SEM), demonstrating that they have formed on the surface of the substrate. Fig. 9b shows a typical region of this sample in which surface precipitates of both types are evident.

The gradual recrystallization of the annealed samples, with higher temperature and longer time, along with the formation of surface precipitates in the final stages of recrystallization are both expected results. The formation of oriented internal grains of yttria is not entirely expected, however, In^+ implanted alumina has been reported as forming a dual phase Al_2O_3/M_2O_3 microstructure as a result of annealing in oxygen [14]. In that study the grains that formed were not oriented and resulted only from a very high temperature anneal (1500 °C). A larger portion of the implantation and annealing studies conducted with alumina substrates report aluminate formation

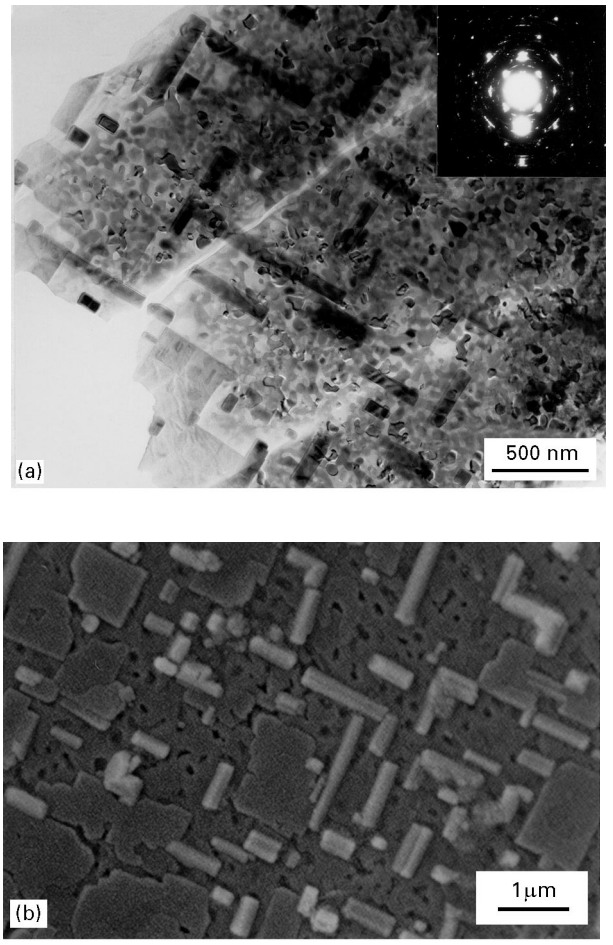

Figure 9 (a) TEM of the 1400 °C, 60 min annealed sample. (b) SEM image of the surface of the 1400 °C, 60 min annealed sample. Note the alignment of both forms of surface precipitates.

(MAl_2O_4 or $MAlO_3$) and either total or partial surface segregation of the implanted material. For example, Ga^+, Zn^+ and Zr^+ are entirely segregated to the surface of the recrystallized substrate where they form $GaAlO_3$, $ZnAl_2O_4$ and ZrO_2, respectively [16]. Mn^+, Ni^+ and Fe^+ on the other hand, form both internal grains of their respective aluminates ($MnAl_2O_4$, $NiAl_2O_4$, $FeAl_2O_4$) and surface precipitates of either the same aluminate or, in the case of iron, Fe_2O_3 [6, 14].

4. Summary

This research has demonstrated that implantation of 150 and 170 keV yttrium ions into a single crystalline alumina substrate to a fluence of 5×10^{16} ions/cm^2 induces the formation of an amorphous surface layer containing finely distributed, fcc, aluminium-rich particles with an average diameter of 12–13 nm. Post implantation annealing treatments gradually recrystallize the substrate with increasing time and temperature. There is, in addition, an evolution in the microstructure of the annealed samples which is summarized in Fig. 11. A small amount of recrystallization (1000 °C, 90 min) is accompanied by the formation of ~25 nm precipitates of metastable Y_3Al in the implanted region. Annealing at 1100 °C for the same

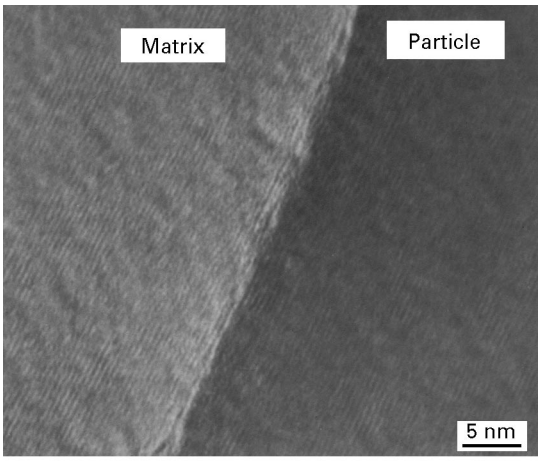

Figure 10 TEM high resolution image of the 1400 °C, 60 min annealed sample, showing coherence of particle with matrix.

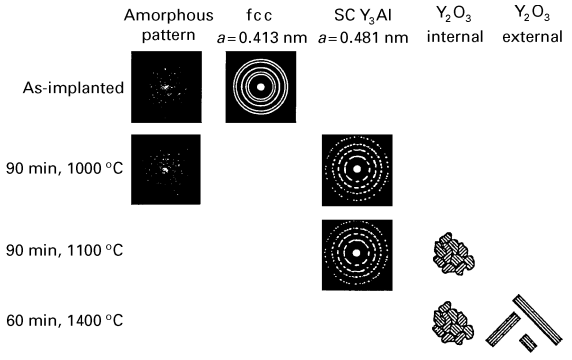

Figure 11 Summary of the microstructures resulting from implantation and annealing.

amount of time results in a microstructure of partially aligned yttria grains embedded in the alumina substrate and the continued existence of the Y_3Al precipitates. Upon total recrystallization of the amorphous layer, the microstructure consists of partially oriented internal grains of yttria as well as larger, faceted rectangular surface grains with aspect ratios ranging from 1:5 to 1:1.5. Both internal and external grains exhibit an orientational relationship with respect to the matrix.

Acknowledgements

This research was sponsored by the Office of Naval Research through the Molecular Design Institute at the Georgia Institute of Technology, by the Engineering Foundation, and by the US Department of Energy under contract no. DE-AC05-96OR 22464 with Lockheed Martin Energy Research Corporation, and through the SHaRE Program under contract no. DE-AC05-76OR 00033 with Oak Ridge Associated Universities. We gratefully acknowledge the contributions of both Dr Neal Evans and Dr David Poker at the Oak Ridge National Laboratory. We thank Dr R. Schwerzle at the Georgia Tech Research Institute, Professor Z. L. Wang and Ms Y. Berta at the Georgia Institute of Technology, and Professor D. I. Potter, J. Koch and L. McCurdy at the University of Connecticut for their assistance.

References

1. C. W. WHITE, D. S. ZOU, J. D. BUDAI, R. A. ZUHR, R. H. MAGRUDER and D. H. OSBORNE, *Mater. Res. Soc. Symp.* **316** (1994) 499.
2. A. P. MOURITZ, D. K. SOOD, D. H. ST JOHN, M. V. SWAIN, J. S. WILLIAMS, *Nuc. Inst. Meth. B* **B19/20** (1987) 805.
3. R. F. HAGLUND Jr., L. YANG, R. H. MAGRUDER, C. W. WHITE, R. A. ZUHR, L. YANG, R. DORSINVILLE and R. R. ALFANO, *ibid.* **B19** (1994) 493.
4. J. ALLEGRE, G. ARNAUD, H. MATHIEU, P. LEFEBVRE, W. GRANIER and L. BONDES, *J. Cryst. Growth* **138** (1994) 998.
5. C. W. WHITE, J. D. BUDAI, S. P. WITHROW, S. J. PENNYCOOK, D. M. HEMBREE, D. S. ZOU, T. VO-DINH and R. H. MAGRUDER, *Mater. Res. Soc. Symp.* **316** (1994) 487.
6. P. S. SKLAD, C. J. McHARGUE, C. W. WHITE and G. C. FARLOW, *J. Mater. Sci.* **27** (1992) 5895.
7. K. FUKUMI, A. CHAYAHARA, H. YAMANAKA, K. FUJII, J. HAYAKAWA and M. SATOU, *J. Non-Cryst. Solids* **163** (1993) 59.
8. A. PEREZ, *J. Mater. Res.* **2** (1987) 910.
9. J. F. ZIEGLER, "Transport of Ions in Matter" (IBM Research 28-0, Yorktown, NY 10598, 1992).
10. D. I. POTTER, J. M. HAMPIKIAN and M. SAQIB, *Mater. Charact.* **28** (1992) 89.
11. P. J. BURNETT and T. F. PAGE, *Rad. Eff.* **97** (1986) 283.
12. *Idem*, *J. Mater. Sci.* **19** (1984) 3524.
13. *Idem*, *ibid.* **20** (1985) 4624.
14. G. C. FARLOW, P. S. SKLAD, C. W. WHITE and C. J. McHARGUE, *J. Mater. Res.* **5** (1990) 1502.
15. C. W. WHITE, G. C. FARLOW, C. J. McHARGUE, P. S. SKLAD, M. P. ANGELINI and B. R. APPLETON, *Nuc. Inst. Meth. B* **B7/8** (1985) 473.
16. E. M. HUNT, J. M. HAMPIKIAN and D. B. POKER, *Mater. Res. Soc. Symp. Proc.* **396** (1996) 403.
17. E. M. HUNT, J. M. HAMPIKIAN and N. D. EVANS, in Proceedings of the 30th Annual Conference of the Microbeam Analysis Society, Minneapolis, MN August, 1996. (San Francisco Preas Inc., San Francisco, CA 1996) p. 534.
18. N. D. EVANS, E. A. KENIK, J. BENTLEY and S. J. ZINKLE, in Proceedings of the 29th Annual Conference of the Microbeam Analysis Society, Kansas City, KS, August, 1995. (Jones & Begell, New York, NY, 1995) p. 309.
19. H. BAKER (Ed), "ASM Handbook 3, Alloy Phase Diagrams" (American Society for Metals International, Metals Park, Ohio, 1992).
20. J. M. HAMPIKIAN, M. SAQIB and D. I. POTTER, *Met. Trans. B* **27B** (1996) 491.
21. D. B. CULLITY, "Elements of X-ray Diffraction" (Addison-Wesley Publishing Co. Inc., Reading, MA, 1978).
22. M. OHKUBO and N. SUZUKI, *Phil. Mag. Lett.* **57** (1988) 261.
23. N. D. EVANS, S. J. ZINKLE and J. BENTLEY, *Mater. Res. Soc. Symp. Proc.* **373** (1995) 419.
24. S. NODA, H. DOI and O. KAMIGAITO, *J. Mater. Res.* **4** (1989) 671.

Received 2 July
and accepted 30 October 1996